



Towards an atomistic understanding of electrocatalytic partial hydrocarbon oxidation: Propene on palladium

Winiwarter, Anna; Silvioli, Luca; Scott, Soren B.; Enemark-Rasmussen, Kasper; Sariç, Manuel; Trimarco, Daniel B.; Vesborg, Peter C.K.; Moses, Poul G.; Stephens, Ifan E.L.; Seger, Brian

Total number of authors:
12

Published in:
Energy and Environmental Science

Link to article, DOI:
[10.1039/c8ee03426e](https://doi.org/10.1039/c8ee03426e)

Publication date:
2019

Document Version
Peer reviewed version

[Link back to DTU Orbit](#)

Citation (APA):

Winiwarter, A., Silvioli, L., Scott, S. B., Enemark-Rasmussen, K., Sariç, M., Trimarco, D. B., Vesborg, P. C. K., Moses, P. G., Stephens, I. E. L., Seger, B., Rossmeisl, J., & Chorkendorff, I. (2019). Towards an atomistic understanding of electrocatalytic partial hydrocarbon oxidation: Propene on palladium. *Energy and Environmental Science*, 12(3), 1055-1067. <https://doi.org/10.1039/c8ee03426e>

General rights

Copyright and moral rights for the publications made accessible in the public portal are retained by the authors and/or other copyright owners and it is a condition of accessing publications that users recognise and abide by the legal requirements associated with these rights.

- Users may download and print one copy of any publication from the public portal for the purpose of private study or research.
- You may not further distribute the material or use it for any profit-making activity or commercial gain
- You may freely distribute the URL identifying the publication in the public portal

If you believe that this document breaches copyright please contact us providing details, and we will remove access to the work immediately and investigate your claim.

Towards an atomistic understanding of electrocatalytic partial hydrocarbon oxidation: propene on palladium

Anna Winiwarter^{a||}, Luca Silvioli^{b||}, Soren B. Scott^a, Kasper Enemark-Rasmussen^c, Manuel Sariç^b, Daniel B. Trimarco^d, Peter C. K. Vesborg^a, Poul G. Moses^e, Ifan E. L. Stephens^f, Brian Seger^a, Jan Rossmeisl^{b*} and Ib Chorkendorff^{a*}

^aSurfCat, Department of Physics, Technical University of Denmark, Fysikvej, Byg. 311, 2800 Kgs. Lyngby, Denmark.

^bNano-Science Center, Department of Chemistry, University of Copenhagen, Universitetsparken 5, 2100 Copenhagen, Denmark

^cDepartment of Chemistry, Technical University of Denmark, Kemitorvet, Byg.207, 2800 Kgs. Lyngby, Denmark

^dSpectro Inlets, COBIS, Ole Maaløes Vej 3, 2200 Copenhagen, Denmark

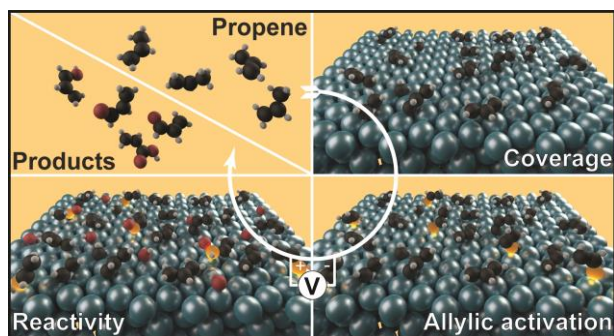
^eHaldor Topsoe A/S, Haldor Topsøes Allé 1, 2800 Kgs. Lyngby, Denmark

^fDepartment of Materials, Imperial College London, Royal School of Mines, London, SW7 2AZ, UK

^{||}these authors contributed equally

*corresponding authors: jan.rossmeisl@chem.ku.dk, ibchork@fysik.dtu.dk

1. Abstract



The efficient partial oxidation of hydrocarbons to valuable chemicals without formation of CO₂ is one of the great challenges in heterogeneous catalysis. The ever-decreasing cost of renewable electricity and the superior control over reactivity qualify electrochemistry as a particularly attractive means of addressing this challenge. Yet, to date, little is known about the factors regulating hydrocarbon oxidation at the atomic level. A relevant showcase reaction is propene electro-oxidation to key industrial commodity chemicals, such as acrolein, acrylic acid and propylene oxide. In this study, we investigate the partial electrochemical oxidation of propene on high-surface area Pd electrodes using

a combination of electrochemical measurements, advanced product characterization and theoretical modelling. We report a new reaction product, propylene glycol, and high selectivity towards acrolein. We further identify key reaction intermediates and propose a mechanism dictated by the surface coverage of organic species formed in-situ, where stable reactant adsorption at low coverage determines the selectivity towards allylic oxidation at high coverage. Our fundamental findings enable advances in partial hydrocarbon oxidation reactions by highlighting atomic surface structuring as the key to selective and versatile electrochemical catalyst design.

Broader Context:

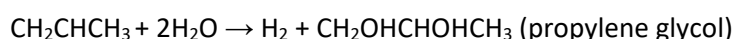
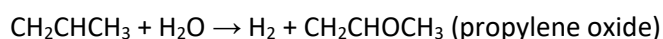
The transition from fossil to renewable energy sources must accelerate to mitigate the devastating effects of climate change. Within this context, society electrification is a highly regarded strategy, in which the industrial sectors are also expected to migrate to electrified manufacturing processes. Many thermocatalytic industrial chemical processes - some established for more than a century - are expensive and energetically inefficient and therefore require modernization. In many cases, electrochemistry has great potential for replacing outdated processes. Electrochemical reactions are inherently safer and allow fine selectivity control in optimized systems. They are also more versatile and scalable, thus suited for decentralization and embedding in national energy grids, which will help compensate renewable energy fluctuations. In particular, a great opportunity lies in optimizing electrochemical partial oxidation reactions, which offer shortcuts to valuable products not accessible in traditional chemical industry due to the tendency of carbon compounds to fully oxidize in thermally driven processes.

Understanding the factors that control electrocatalytic reactions at the atomic level is the first step to creating efficient large scale electrochemical processes. Our work provides fundamental insights into the mechanism of hydrocarbon electro-oxidation through the study of a model, yet industrially relevant, reaction of partial propene oxidation.

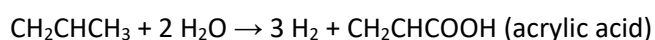
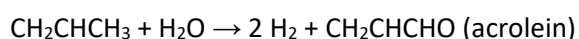
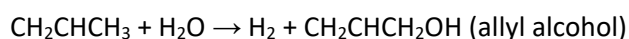
2. Introduction

Wind and solar energy are increasingly outcompeting fossil fuels for electricity generation.¹ Increasing renewable electricity output calls for the electrochemical production of commodity chemicals, such as alcohols, aldehydes and acids.²⁻⁴ Selective direct oxidation of hydrocarbons to partially oxidized products while avoiding full oxidation to CO₂, the most thermodynamically favored product, remains elusive in gas phase heterogeneous catalysis.⁵⁻¹¹ Compared to thermal heterogeneous catalysis, an electrochemical approach to selective partial oxidation can be advantageous. Mild oxidizing conditions and fine control over reaction parameters could direct the reaction to one specific product while preventing the formation of CO₂.¹²⁻¹⁴ At the same time, electrochemical reactors based on fuel cell technology would allow for decentralized production with flexible feedstocks.¹⁵

Propene is an interesting model molecule for studying mechanisms concerning hydrocarbon selective oxidation. It provides two different reaction sites: the C-C double bond (vinyl group) and the allyl carbon. Oxidation of the double bond leads to the formation of 1,2-propylene oxide, which is hydrolyzed to propylene glycol in aqueous environment.¹⁶



The allylic carbon, on the other hand, can be oxidized to produce allyl alcohol, acrolein, and acrylic acid.¹⁷



The structures of propene and relevant oxidation products are reported in Figure 1.

High annual production capacities for several partial oxidation products of propene highlight the importance of this reaction; examples are propylene oxide (9.81 Mt, 2016)¹⁸, propylene glycol (2.56 Mt, 2017 prognosis)¹⁹, and acrylic acid (7.66 Mt, 2016).¹⁸ Acetone, despite annual production volumes in the same order of magnitude as those mentioned²⁰, is not considered hereafter a desired product, as it does not form electrocatalytically in our reaction system.


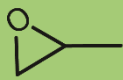
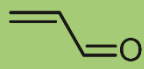
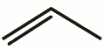
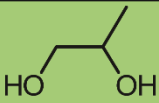
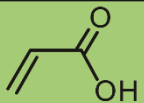
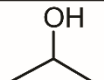
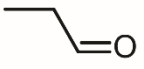
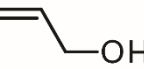

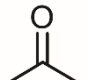
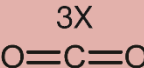
 Name Rev. Pot. (V/RHE) n ^o e	 1,2-propylene oxide (2-methyloxiran) 2 0.66	 Acrolein (prop-2-en-1-al) 4 0.25
 Propene 0 NA	 Propylene glycol (propan-1,2-diol) 2 0.41	 Acrylic acid (prop-2-enoic acid) 6 0.19
 Isopropanol (propanol) 0 NA	 Propionaldehyde (propanal) 2 0.15	 Allyl alcohol (prop-2-en-1-ol) 2 0.38
 Propane -2 0.51	 Acetone (propanon) 2 0.00	 3X Carbon dioxide 18 0.10

Figure 1 - Overview over propene and its main derivatives. A green background highlights industrially relevant products, while red denotes undesired compounds. The thermodynamic reversible potential for formation by propene oxidation was calculated from the reaction free energy, including solvation for all liquid products. Calculations details are reported in the SI.

A few prior studies have examined the direct electrochemical oxidation of propene.^{21–27} The most promising results have been reported on palladium electrodes in acidic environment. Stafford²⁸ reported acrolein, acrylic acid, acetone and CO₂ as the main products on palladium in acidic aqueous electrolyte. Otsuka et al.²⁹ used a fuel cell set-up and found mainly acrolein and acrylic acid at lower cell voltage, but increasing amounts of acetone and CO₂ at higher cell voltage. However, neither of these studies provide a full picture of faradaic efficiency *versus* potential, nor do they propose a mechanistic explanation for the observed selectivity towards allylic oxidation.

Herein, we present a systematic study of propene oxidation on high surface area palladium electrodes. We use dilute HClO_4 as electrolyte, known to be non-interacting with the electrode, to decouple electrolyte effects from surface dynamics.³⁰ We differentiate the electrocatalytic pathway from non-electrochemical side reactions, confirming that acetone is produced by homogeneous reaction with Pd^{2+} .^{28,29} We report the identification of a key electrochemical reaction intermediate, allyl alcohol, as well as an additional product, propylene glycol, which to the best of our knowledge has not been reported on this catalyst before. Using a combination of density functional theory (DFT) modelling and electrochemical mass spectrometry (EC-MS), we provide fundamental insights into the mechanism governing the changes in product distribution with potential in bulk experiments. The surface coverage plays a crucial role in steering oxidation activity and selectivity: surface chemistry under reaction conditions forces reactants to weaker adsorption configurations, enabling selective oxidation of the allyl carbon.

3. Experimental methods

Deposition of porous Pd

High surface area Pd electrodes were prepared by electrodeposition on glassy carbon sheets (1x1.5 cm, HTW-Germany) or on glassy carbon disks (5 mm diameter, Pine Instruments) for the EC-MS measurements. The sheets/disks were initially thoroughly polished with $\frac{1}{4}$ μm diamond on a polishing cloth (Struers). Before each experiment the glassy carbon electrodes were cleaned from metal contaminations by immersion in aqua regia, followed by repeated rinsing and sonication in ultrapure water. For electrical contact, a Pt wire was attached to the glassy carbon and wrapped in Teflon tape to prevent contact with the electrolyte. The Pd deposition was carried out using a 2 mM PdCl_2 solution (99.999%, Sigma Aldrich) in 2 M H_2SO_4 (suprapur, Merck) in a 2-electrode setup with a Pt mesh (99.9%, GoodFellow) as a counter electrode. For optimal adhesion, a thin Pd layer was deposited at -1 V vs the counter electrode for 1 min, followed by deposition at -4 V vs counter for 3 min with simultaneous H_2 evolution (hydrogen bubble template method)^{31,32}. The electrode was thoroughly rinsed with ultrapure water before further use.

Electrochemical experiments

Electrochemical experiments with product analysis were carried out in a 3-electrode setup in a 3-compartment glass cell (H-cell, see Figure 2), as described previously.³³ The electrolyte was prepared by dilution of concentrated HClO_4 (suprapur, Merck) in ultrapure water (18.2 M Ω resistivity, Millipore, Synergy UV system). A Pt mesh counter and a Hg/HgSO₄ reference electrode were employed. The reference electrode was calibrated regularly *versus* the RHE scale by measuring the open circuit voltage (OCV) at a Pt electrode in H₂ saturated electrolyte until stable for at least 10 minutes. Gases (Ar 5.0, AGA or Propene 4.0, BOC) were supplied through a glass frit, connected to a gas loop allowing for circulation of the gas during the reaction. Additional experiments were carried out in a conventional RDE setup.

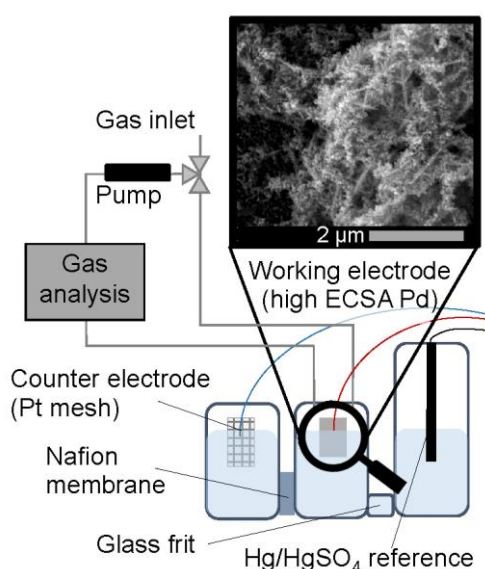


Figure 2 - Schematic of the 3-compartment cell used for bulk oxidation experiments. The inset shows a SEM image of a high surface area palladium electrode.

For each measurement, a freshly prepared sample was placed in electrolyte and held at 0.4 V vs RHE while the electrolyte was purged with propene. No electrochemical reaction is observed at this potential. The potential was then stepped up to the potential of interest and held for one hour.

The electrochemical surface area (ECSA) was determined after each experiment, using the PdO reduction peak in cyclic voltammograms. These CVs were carried out in fresh electrolyte. Rather than

assuming oxidation of a full monolayer of Pd, we calibrated the charge from PdO reduction with CO stripping experiments on the same electrode (for details see the SI).

All glassware was cleaned with aqua regia before use.

Product analysis

Gaseous products were determined by gas chromatography (GC). Different methods were used for liquid products characterization: static headspace gas chromatography (HS-GC) for acetone and propanal, high pressure liquid chromatography (HPLC) for acrolein and acrylic acid, and quantitative nuclear magnetic resonance spectroscopy (qNMR) for allyl alcohol, isopropanol and propylene glycol. The Pd concentration in the electrolyte was determined with inductively coupled plasma-mass spectrometry (ICP-MS). For experimental details, see SI.

EC-MS

For electrochemistry-mass spectrometry (EC-MS) measurements, we used the setup and methodology described previously.³⁴ This setup uses a membrane microchip to interface the electrochemical environment and the vacuum system containing the mass spectrometer. CO and propene stripping experiments involved (1) dosing the reactant gas (CO or propene) through the membrane chip while holding the electrode at constant potential, (2) flowing He through the chip until the mass spectrometer signal for the reactant gas returned to baseline, and (3) cycling the electrode potential. All EC-MS measurements were performed in 1.0 M HClO₄ in order to have sufficient electrolytic conductivity through the thin layer of electrolyte. Mass spectrometer signals were converted to amounts of propene, propane, and CO₂ using internal calibration measurements (see SI for details).

DFT calculations

All ground state DFT and climbing image nudged elastic band (NEB) calculations were performed with the Grid-based Projected Augmented Wave (GPAW) program and the Atomic Simulation Environment (ASE) package.^{35–37} The Kohn-Sham wavefunctions are represented in real-space uniform grids (finite

difference mode); we used the BEEF-vdW exchange and correlation functional, a grid spacing of 0.18 Å and k-point sampling of (2x2x1). For NEB calculations, the RPBE exchange and correlation functional were used instead to quantify the energy gap between initial and transition state in reaction chemical steps. More computational details and Information on structures and reference compounds are reported in the SI.

4. Results and Discussion

Electrocatalytic activity

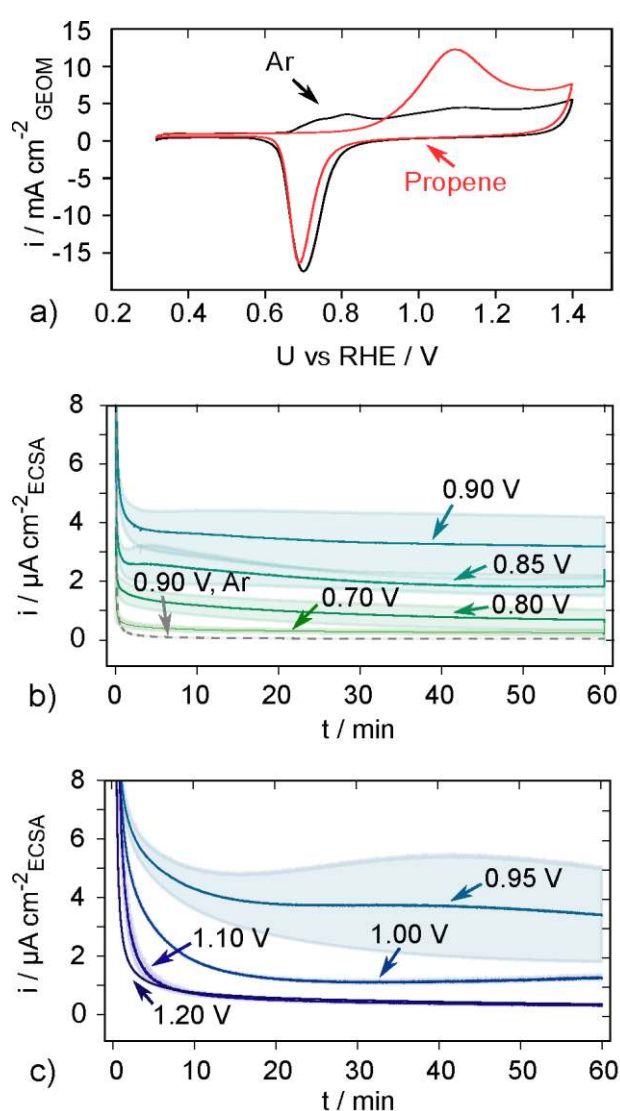


Figure 3 - a) Cyclic voltammograms (stable) of high surface area Pd in 0.1 M HClO₄ saturated with Ar (black) and propene (red), respectively, recorded at a scan rate of 50 mV/s in a rotating disc electrode setup (no rotation) while purging with gas. b) and c) Current-time traces of propene oxidation at constant potentials in 0.1 M HClO₄: average and standard deviations of three ($E \leq 0.95 \text{ V}$) or two ($E = 1.0 \text{ V}, 1.1 \text{ V}$) electrodes and a single, representative experiment for 1.2 V. The current-time trace in Ar saturated electrolyte at 0.9 V vs RHE is shown for comparison. b) mildly oxidizing potentials, c) strongly oxidizing potentials.

Cyclic voltammograms (CVs) of high surface area Pd in Ar and propene saturated 0.1 M HClO₄ are shown in Figure 3a (black and red line, respectively). The onset of Pd oxidation is at ca. 0.65 V vs RHE; two oxidation waves can be distinguished with peaks around 0.8 and 1.1 V vs RHE, suggesting a range of different facets are present on the Pd electrode.^{38–41} In the cathodic scan a sharp reduction peak is present at ca. 0.7 V vs RHE, where PdO is reduced. In propene saturated HClO₄ the onset of oxidative current is shifted significantly to almost 0.9 V vs RHE, followed by an oxidative peak with a significantly higher peak current than in Ar at a potential of ca. 1.1 V vs RHE. We attribute this peak to be the oxidation of propene in addition to PdO formation. The PdO reduction peak area is similar in the presence of propene, supporting the interpretation that the increased current in the anodic scan is in fact irreversible oxidation of propene rather than increased surface oxidation, as the latter would also manifest in a more pronounced reduction peak.

In order to investigate the selectivity for different products, we carried out chronoamperometry experiments in 0.1 M HClO₄. Products were accumulated for 1 h at constant potential in order to reach high enough product concentrations for reliable product detection (see Methods Section for details). ECSA normalized current-time traces recorded during product accumulation are shown in Figure 3b and c. In all cases, a significant initial current drop is observed. For a more detailed analysis of the current-time traces, see Figure S4. The highest current densities are observed at 0.90 and 0.95 V vs RHE. At the same potentials, the variation between the individual experiments are also the largest. With the equilibrium potential for the oxidation of Pd at pH 1 being 0.91 V vs RHE⁴², the high variability at these potentials is presumably related to the instability of the catalyst due to the surface redox and/or dissolution processes, which may modify the surface area to an unknown degree. The drop in current density at potentials larger than 0.95 V vs RHE can be explained by the formation of passivating PdO on the surface.

Product distribution and potential

Primary oxidation products

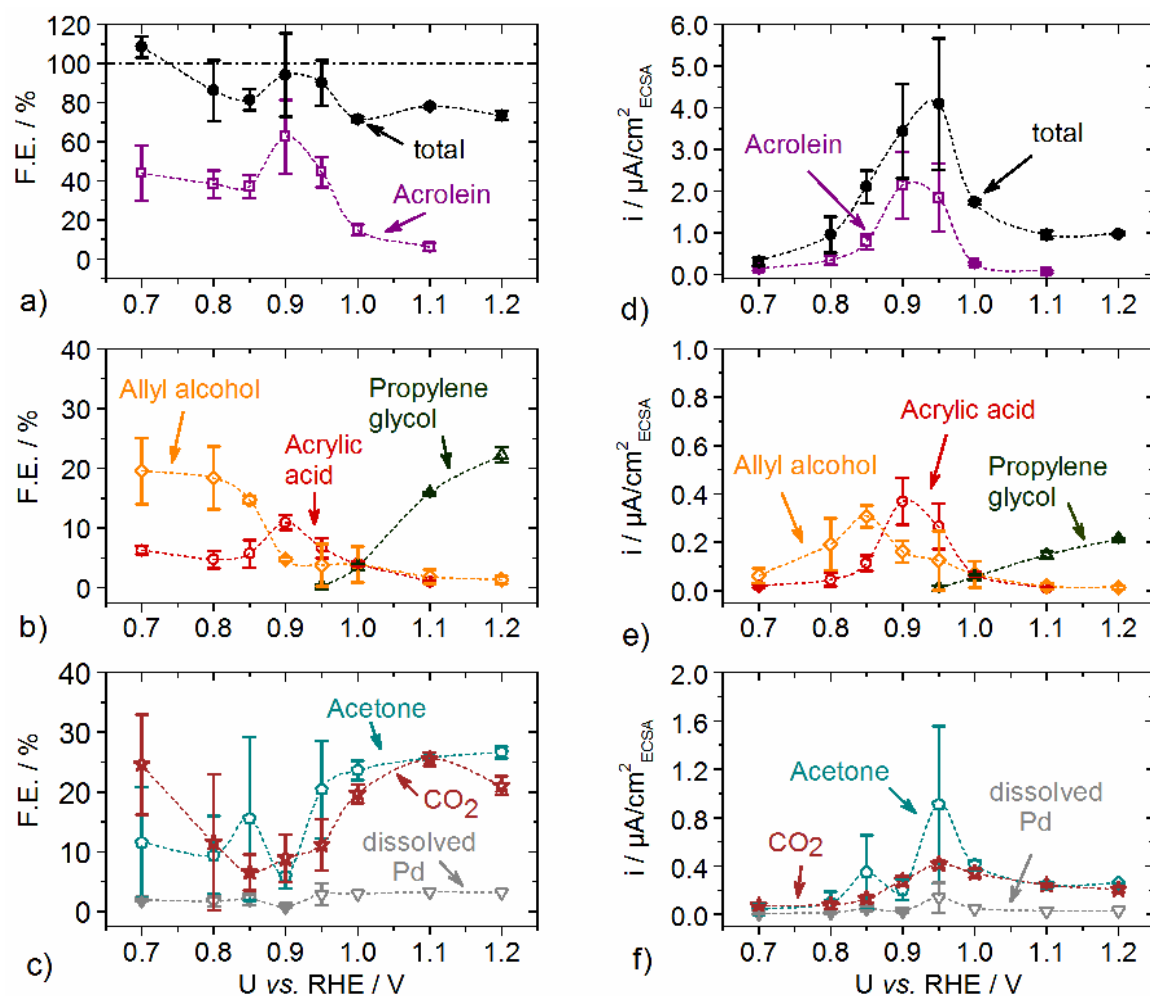


Figure 4 - Product distribution from chronoamperometry experiments presented in Figure 3 b-c) as a function of potential: a- c), faradaic efficiencies; d- f), partial current densities. Additional undenoted products were propanal (concentration unreliable as close to the quantification limit, see SI) and isopropanol (chemical product, see text).

Figure 4 shows the propene oxidation activity and product distribution as a function of potential. The faradaic efficiencies and partial current densities are shown for various products in Figure 4a-c, and Figure 4d-f, respectively. The current was calculated based on the concentration at the end of the 1-hour period. For better readability, the products are divided into three groups: The main target product acrolein, other propene oxidation products of interest (allyl alcohol, acrylic acid and propylene glycol), and undesired side products (acetone, CO₂ and dissolved Pd).

Partial current density and faradaic efficiency for acrolein production are highest in the middle of the potential range studied, with maxima of $2.1 \mu\text{A}/\text{cm}^2$ and 62 %, respectively, at 0.9 V vs RHE. At potentials above 1.1 V vs RHE the concentration was too low for quantification. The trends for acrylic acid follow those for acrolein, reaching a maximum faradaic efficiency of 11 % at 0.9 V vs RHE. Allyl alcohol shows a similar dependency, except that the peak maximum is shifted to 0.85 V vs RHE. Propylene glycol, on the other hand, is only produced at 1.0 V vs RHE and more anodic, and both specific current density and faradaic efficiency increase with increasing anodic potential. In addition to the mentioned products, small amounts of propanal were observed, but were too small to measure quantitatively (see Figures S14 and S25). The non-electrochemical product isopropanol was also observed in small quantities (1% of liquid products by mol at 0.9 V vs RHE).

We attribute high standard deviation in product faradaic efficiency below 0.9 V vs RHE to the lack of significant quantities of products (see SI); however, at 0.9 and 0.95 V vs RHE we hypothesize the error is caused by the instability of the catalyst due to oxidation and dissolution processes as discussed above.

The overall faradaic efficiency considering only propene oxidation products is significantly less than 100% at strongly oxidizing potentials (Figure 4), which may partially relate to oxidation of the surface and corrosion of the catalyst. Based on the charge required for the formation of one monolayer PdO (Figure S4) we estimated that at potentials more anodic than 0.95 V vs RHE, Pd oxidation can account for up to 10-15 % faradaic efficiency, increasing the total faradaic efficiency to at least 90%.

Homogeneous reactions

We noted undesired side reactions are taking place in the electrolyte. The acid catalyzed hydration of propene to isopropanol in the presence of water is well known⁴³ and was also observed in the electrolyte after purging with propene without an electrode (see SI). Separate experiments with isopropanol added directly to the electrolyte showed no activity for electrochemical oxidation of the alcohol, excluding this compound from the primary reaction mechanism.

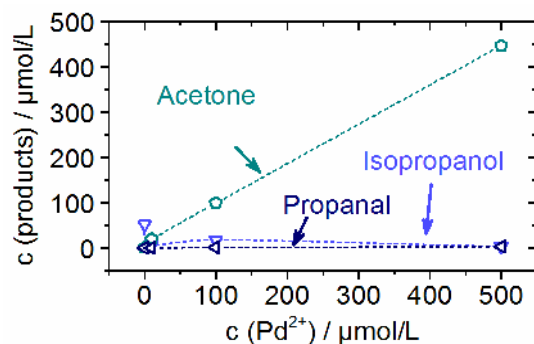


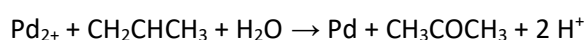
Figure 5 - Homogeneous reaction of propene in 0.1 M HClO₄ with different concentrations of PdCl₂. All products formed under these conditions are shown in the figure.

Previous studies on this system have reported homogeneous side reaction with Pd²⁺ in solution.^{28,29}

The concomitant increase of acetone concentration with Pd-ion concentration throughout the experiments suggests a direct relationship. In order to verify the role of Pd²⁺ as a catalyst/reactant for the oxidation to acetone, we analyzed the products formed when purging propene through a 0.1 M HClO₄ solution containing different concentrations of Pd²⁺ ions (Figure 5).

The concentration of the main product acetone linearly increases with Pd concentration with a slope close to one, indicating the role of Pd²⁺ in acetone production and suggesting that the Pd²⁺ ions are fully consumed within the reaction time. For Pd²⁺ concentrations of 100 μM and above, the formation of metal nanoparticles was evident from discoloration of the solution and formation of precipitate.

The reaction is expected to proceed through a Wacker-type mechanism as follows ($\Delta G = -167$ kJ/mol):²⁹



While closing the catalytic cycle by re-oxidation of Pd at the electrode has been proposed²⁹, we did not see evidence for this in our system (see Figure S26). Therefore we do not consider acetone as a desirable product.

Product stability

Degradation of products before quantification resulting in underestimation of the amounts produced could explain the low total Faradaic efficiencies in Figure 4a. We therefore followed

changes in product concentrations with time after the end of the experiment. We observed a significant decrease in acrolein concentration over time, which we could assign to the formation of hydration products 3-hydroxypropanal and propane-1,3,3-triol (see SI). Despite our efforts to quantify acrolein and acrylic acid as fast as possible using HPLC, this might lead to a slight underestimation in their quantification.

Surface chemistry and mechanistic analyses

In the following, we rationalize the observations in bulk oxidation tests with mechanistic analyses by means of DFT modelling and propene stripping experiments, proposing a reaction mechanism for the potential window in which the catalyst surface is metallic. We further provide insights into the relationship between surface population and catalytic activity, highlighting the correlation of surface coverage with the reaction outcome.

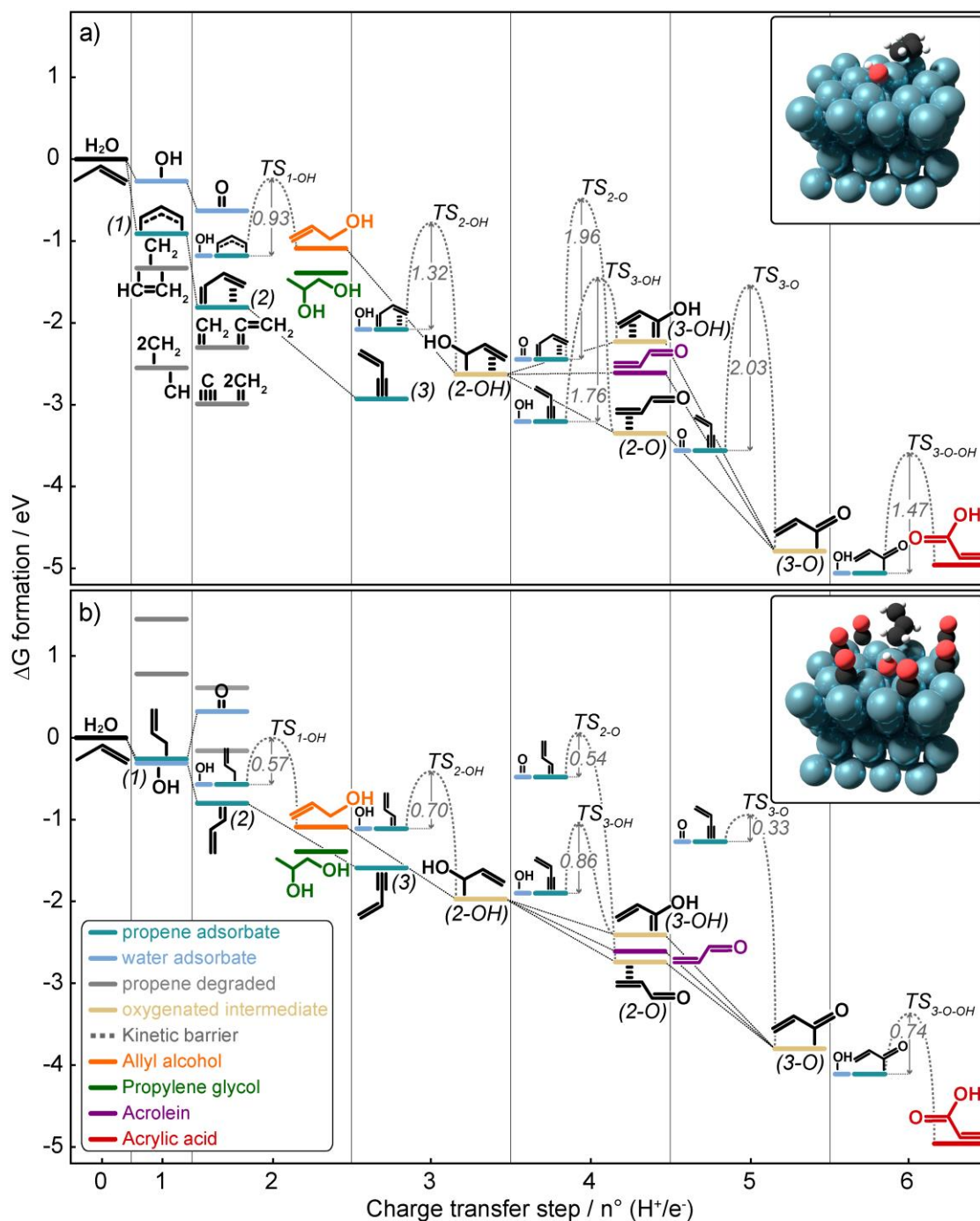


Figure 6 - Proposed reaction scheme for propene oxidation in water on a) clean Pd fcc(111) surface and b) 6*CO poisoned Pd fcc(111). The DFT Gibbs energy of formation for adsorbed intermediates and transition states at $U = 0.9$ V vs RHE are given as a function of the number of H^+/e^- couples exchanged with the system. We assign labels in brackets to all intermediates for easier referencing in the text. The graphical insets provide visual examples of the model catalyst surface with adsorbates.

Surface species, intermediates and reaction pathway - DFT

Figure 6 shows the energies of propene oxidation products, intermediates and transition states relative to water, propene, and the palladium fcc(111) surface, calculated by DFT and adjusted to +0.9 V vs RHE

using the computational hydrogen electrode reference system.⁴⁴ For the energy levels at 0.0 V vs RHE, see Figure S29. Figure 6a reports the reaction energetics as calculated on a clean Pd slab (termed *clean*), while Figure 6b shows the energy for the same intermediates adsorbed on a Pd slab with high surface coverage, mimicked by six CO spectator molecules adsorbed per unit cell (termed *CO poisoned*), contouring the intermediates adsorption site(s). In Figure 6, in addition to the energies of the intermediates, we report the initial states for chemical oxidation steps as half light/half teal blue lines, with energy values corresponding to the sum of the respective adsorbates' energy, and the calculated gas phase product reversible potentials. The kinetic reaction barriers are represented by dashed curves linking initial, transition and final states. The other dashed lines between intermediates indicate an elementary step of a (H^+/e^-) couple loss with negligible kinetic barrier.

The first catalytic step in propene electro-oxidation is adsorption of propene. Comparing the possible adsorption geometries, we find that adsorption via deprotonation of the allyl carbon is the most favorable for the potential range of interest (Figure S27, blue bars); additionally, propene activation in allylic position is conformal with the observed product distribution. We therefore focus the mechanistic analysis on propene oxidative adsorption and reactivity via allylic carbon activation, followed by reaction with adsorbed $*OH$ or $*O$. In Scheme 1, we report the elementary steps considered in the mechanistic study.

Elementary step	$\Delta G[\text{eV}]@0.9V_{\text{RHE}}$	
	Clean	CO poisoned
$\text{CH}_3\text{CHCH}_2 + * \rightarrow * \text{CH}_2\text{CHCH}_2 + (\text{H}^+/\text{e}^-)$ (propene) (1)	-0.91	-0.26
$* \text{CH}_2\text{CHCH}_2 \rightarrow * \text{CHCHCH}_2 + (\text{H}^+/\text{e}^-)$ (1) (2)	-0.90	-0.54
$* \text{CHCHCH}_2 \rightarrow * \text{CCHCH}_2 + (\text{H}^+/\text{e}^-)$ (2) (3)	-1.13	-0.79
$\text{H}_2\text{O} + * \rightarrow * \text{OH} + (\text{H}^+/\text{e}^-)$	-0.27	-0.31
$* \text{OH} \rightarrow * \text{O} + (\text{H}^+/\text{e}^-)$	-0.36	0.64
$* \text{CH}_2\text{CHCH}_2 + * \text{OH} \rightarrow \text{CH}_2(\text{OH})\text{CHCH}_2 + 2*$ (1) (allyl alcohol)	0.09 [†]	-0.52 [†]
$* \text{CHCHCH}_2 + * \text{OH} \rightarrow * \text{CH}(\text{OH})\text{CHCH}_2 + *$ (2) (2-OH)	-0.55 [†]	-0.86 [†]
$\text{CH}_2(\text{OH})\text{CHCH}_2 + * \rightarrow * \text{CH}(\text{OH})\text{CHCH}_2 + (\text{H}^+/\text{e}^-)$ (allyl alcohol) (2-OH)	-1.54	-0.88
$* \text{CH}(\text{OH})\text{CHCH}_2 \rightarrow * \text{C}(\text{OH})\text{CHCH}_2 + (\text{H}^+/\text{e}^-)$ (2-OH) (3-OH)	0.40	-0.44
$* \text{CH}(\text{OH})\text{CHCH}_2 \rightarrow \text{CHOCHCH}_2 + *$ (2-OH) (acrolein)	0.02	-0.64
$* \text{CH}(\text{OH})\text{CHCH}_2 \rightarrow \text{CHOCH}^* \text{CH}_2 + (\text{H}^+/\text{e}^-)$ (2-OH) (2-O)	-0.72	-0.77
$* \text{CHCHCH}_2 + * \text{O} \rightarrow \text{CHOCH}^* \text{CH}_2 + *$ (2) (2-O)	-0.92 [†]	-2.26 [†]
$* \text{CCHCH}_2 + * \text{OH} \rightarrow * \text{C}(\text{OH})\text{CHCH}_2 + *$ (3) (3-OH)	0.97 [†]	-0.51 [†]
$\text{CHOCH}^* \text{CH}_2 \rightarrow \text{CHOCHCH}_2 + *$ (2-O) (acrolein)	0.74 [†]	0.13 [†]
$* \text{CCHCH}_2 + * \text{O} \rightarrow * \text{COCHCH}_2 + *$ (3) (3-O)	-1.23 [†]	-2.53 [†]
$* \text{C}(\text{OH})\text{CHCH}_2 \rightarrow * \text{COCHCH}_2 + (\text{H}^+/\text{e}^-)$ (3-OH) (3-O)	-2.56	-1.39
$\text{CHOCH}^* \text{CH}_2 \rightarrow * \text{COCHCH}_2 + (\text{H}^+/\text{e}^-)$ (2-O) (3-O)	-1.44	-1.06
$* \text{COCHCH}_2 + * \text{OH} \rightarrow \text{COOHCHCH}_2 + 2*$ (3-O) (acrylic acid)	0.10 [†]	-0.85 [†]

[†] energy of chemical step, potential independent

Scheme 1- Reaction elementary steps with relative free energy variation at 0.9V vs. RHE for clean (Figure 6a) and CO poisoned (Figure 6b) catalytic substrate. The labels and colors correspond to those in Figure 6.

The consideration of elementary steps whereby adsorbed propene reacts with *OH and *O (Langmuir-Hinshelwood mechanism) is motivated by different factors. First, the onset of significant propene oxidation activity at about 0.7 V vs RHE (Figure 4) corresponds well with the DFT-calculated OH

adsorption energy and OH adsorption features in the cyclic voltammogram in argon (Figure 3a). Second, the calculated adsorption energy of propene through the allyl carbon is significantly more exergonic than *OH adsorption, suggesting the reason for the observed low activity is palladium stronger affinity toward carbon as compared to oxygen. Third, the *OH adsorption features of the cyclic voltammograms in Figure 3a are suppressed in propene until the onset of propene oxidation, implying that water activation is limiting the working potential window and that *OH adsorption is required for the oxidation of propene. This kind of competitive adsorption of two Langmuir-Hinshelwood reactants is familiar from CO electro-oxidation on platinum.^{34,45,46}

The suppression of surface oxidation in the presence of propene also justifies our modeling of the reaction on metallic palladium fcc(111). Moreover, this facet has the lowest surface energy of all Pd surfaces, so we expect it to be the most abundant facet on polycrystalline Pd.⁴⁷ As explained in greater details later, reactivity is limited by strong binding of propene, so we omit modeling facets more reactive than (111) as they would perform poorer in the reaction mechanism presented. Instead, we model the reaction by poisoning the catalyst with CO (Figure 6b), to limit surface sites accessibility and investigate the mechanism with destabilized intermediates.

Allylic propene adsorption on Pd begins with *CH₂CHCH₂ (**1**), which further deprotonates to *CHCHCH₂ (**2**) or *CCHCH₂ (**3**), if sites are available. The intermediates adsorb by atop, bridge and 3-fold hollow geometries, respectively; (**1**) and (**2**) are significantly stabilized on the clean surface through coordination of the vinyl group (Figure S27). At high surface coverage (Figure 6b), vinylic coordination is hindered as it requires greater site availability than bare allylic adsorption. Adsorbed propene degradation is favorable on clean Pd (Figure 6a), yielding adsorbed C1 and C2 species as reported with grey lines in Figure 6 (most thermodynamically favored degradations) and Figure S28 (all degradation products). Similarly as for vinylic coordination, we observe that on the poisoned surface the degradation is inhibited, i.e. the energy levels for C1 and C2 species shift upwards relative to adsorbed propene. At the theoretical potential for water activation (0.7 V vs RHE), *O and *OH calculated

adsorption energies are roughly equivalent and the two coexist on the surface. At increasingly anodic potentials, *O coverage progressively replaces *OH on clean Pd, while on CO poisoned surface *OH remains the most stable source of oxygen over a wide potential range. For potentials higher than 1.1 V vs RHE, experimentally we observe a significant activity drop, presumably because of catalyst surface oxidation with a different reaction mechanism involved, whose modeling is beyond the scope of this report.

At potentials above water activation (> 0.7 V vs RHE), we cannot exclude a contribution from *OH and *O to propene proton abstraction; nonetheless we do not anticipate this phenomenon to make a significant contribution to the reaction mechanism: both theoretical simulations and electrochemical mass spectrometry (see below) suggest the oxidative adsorption of propene to occur at much more cathodic potentials.

We then investigate the kinetic barriers to products, calculating the relevant transition state energies on clean and CO poisoned Pd. We find significant activation barriers for all coupling steps between adsorbed propene and *O or *OH, which we consider the reaction rate determining steps. Their transition states can be safely modelled since they all are potential independent, chemical reaction steps. In general, we predict high energy barriers if the intermediates react on a clean Pd surface, as reported in Figure 6a. For **(1) + OH** coupling, required to form allyl alcohol, we calculate an activation energy close to 1eV, which we consider virtually unsurmountable at the experimental conditions tested. For all other steps, the kinetic barriers are even higher: For oxidation of **(2)** *CHCHCH₂ and **(3)** *CCHCH₂, we find an unfavorable activation energy for oxygen incorporation of around 2eV, both with *O and *OH. Besides, **(3)** is an intermediate that cannot convert to the primary product acrolein, as all allylic protons are lost. While **(3)** in theory can react to acrylic acid, its strong interaction with the surface should block its participation in the reaction mechanism.

However, the reaction energetics significantly change if the adsorption geometry of adsorbates is restricted due to the high surface coverage modeled with *CO. The intermediates binding energies on

model CO poisoned surface are significantly weakened (Figure 6b), while the transition states' energetics are only marginally affected. Such selective destabilization results in the critical attenuation of the kinetic barriers, allowing for the reaction to proceed at room temperature. Similarly, adsorbed intermediates are destabilized relative to desorbed products, enabling an exergonic pathway to final products.

In propene electro-oxidation, a mechanistic model that neglects the effects of surface coverage has evident limitations, as it cannot explain the observed products distribution. By comparison between clean surface and *CO hindered reactivity, we propose that propene electro-oxidation to allyl alcohol, acrolein and acrylic acid is enabled only at high surface coverage regimes. Notably, strong energetic drivers to propene degradation on clean Pd suggests not all the adsorbates are oxidized to a desorbing product, increasing the surface population. To test experimentally whether there is a high surface coverage under reaction conditions, we performed propene stripping experiments.

Probing surface population – propene stripping

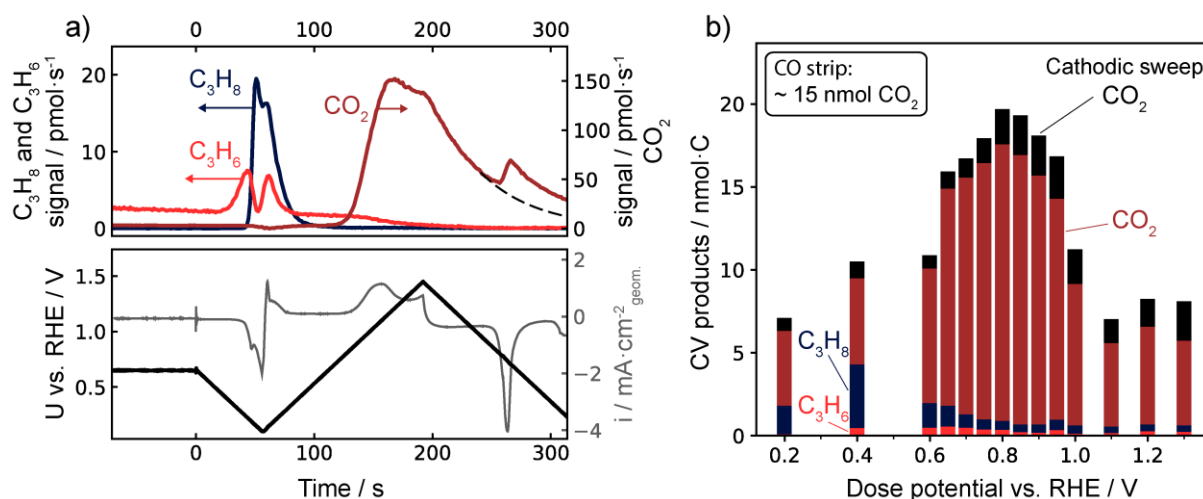


Figure 7 - Propene stripping experiments: a) EC-MS plot of propene stripping. Propene has been dosed and purged at a dose potential of 0.65 V vs RHE. Starting at $t=0$, the potential is scanned cathodic to 0.1 V vs RHE and then cycled between 0.1 V vs RHE and 1.4 V vs RHE while the desorption products propene (C_3H_6), propane (C_3H_8), and CO_2 are monitored. b) The amount of carbon desorbed in the form of the three observed desorption products during the first full cycle of the stripping experiments is plotted as a function of the potential at which propene was dosed. CO_2 evolving during the first anodic and the subsequent cathodic scan is quantified separately as indicated.

We carried out propene stripping experiments in an electrochemistry - mass spectrometry (EC-MS) setup to test for the presence of surface adsorbates under reaction conditions. Figure 7a shows the result of a propene stripping experiment as an EC-MS plot³⁴, with calibrated mass spectrometer signals (propene=C₃H₆ at $m/z=41$, propane=C₃H₈ at $m/z=29$, and CO₂ at $m/z=44$) in the upper panel, and electrochemistry data in the lower panel. The propene is dosed before $t=0$ while the electrode is held at a constant dose potential (here +0.65 V vs RHE) and then purged from the solution. The potential was then cycled, first cathodic to +0.1 V vs RHE and then anodic to +1.4 V vs RHE, while gaseous products were monitored with a mass spectrometer. The majority of desorption products come off during this first cycle (Figure 7a). Thereafter, the electrode is cycled several times (see Figure S10), and the electrolyte is replaced to ensure a clean system for the next propene dose. This procedure was then repeated changing the dose potential.

Propene and propane desorb on the initial cathodic sweep, and CO₂ desorbs on the subsequent cathodic and anodic sweeps. Propene desorption likely represents propene in weak adsorption geometries which can be displaced by surface hydrogen adsorption. Propane is presumed to derive from the hydrogenation of propene adsorbed through vinylic coordination. The dip in propene signal at the cathodic potential limit may indicate that weakly-adsorbed propene can also be reduced with sufficient overpotential. CO₂ desorption after the initial cathodic sweep indicates the presence of strongly bound adsorbates, which cannot be displaced by *H or reduced to propane. Interestingly, a secondary CO₂ peak is observed on the subsequent cathodic scan, as has been observed previously in allyl alcohol stripping experiments.^{48,49} A small amount of CO may have also been observed as a desorption product for some of the stripping experiments, but is challenging to quantify due to interference from both propane and CO₂ at its primary mass fragment, $m/z=28$. In cyclic voltammetry without propene dosing, a much smaller amount (<5% ML) of CO₂ is observed on each anodic sweep and attributed to oxidation of residual carbon contaminations from air.

It should be noted that the EC-MS setup used here is not sensitive towards non-volatile, liquid products. Based on Figure 4, we expect that significant liquid products are produced while propene is dosed for dosing potentials in the range 0.8-1.0 V vs RHE. However, since the adsorbates remaining on the surface after propene is purged already had the chance to form liquid products, we expect that the formation of liquid products during the stripping experiment itself is minor. Figure 7b shows the integrated amount of each desorption product from successive propene stripping experiments as a function of the potential at which the propene was dosed. The products are added together based on the number of carbon atoms so that their proportions represent the portion of the adsorbed propene resulting in each stripping product. A broad maximum in the total amount of desorbates is observed in the range 0.7-0.9 V vs RHE, where the primary desorption product is CO₂. The coverage (on a carbon-atom basis) in this potential range exceeds the saturation coverage of CO based on a CO stripping experiment on the same electrode (Figure S9). This confirms that under steady-state electrolysis, the electrode surface is largely poisoned by strongly-bound adsorbates, as predicted by the DFT model.

Vinyl- vs. allyl-carbon adsorption mechanism

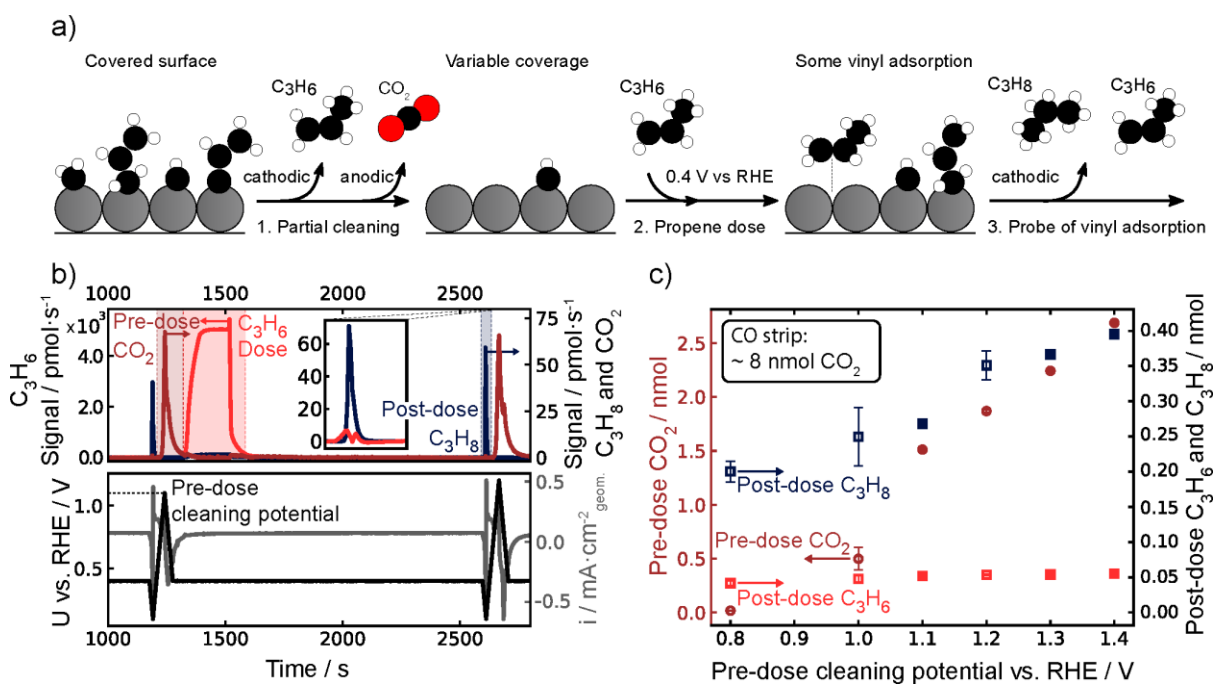


Figure 8 - EC-MS plot of propene stripping "site evacuation" experiments. A surface, which has previously been covered by adsorbates by propene dosing (at $t=0$), is cleaned by scanning to an anodic potential (cleaning potential), stripping a portion of the strongly-adsorbed species off as CO₂. Propene is then dosed again and purged, and the sample is scanned cathodic to 0.1 V vs RHE and back before starting the next experimental sequence. a) Schematic. b) Experimental data. The inset shows

a zoom-in on the signals for propene and propane during the post-dose scan. c) The integrated flux of CO₂ (circles) from the scans prior to and C₃H₈ and C₃H₆ (squares) from the scans after each propene dose are plotted against cleaning potential, which is stepped up and down. For values repeated while stepping down the cleaning potential (0.8, 1.0, and 1.2 V vs RHE), the marker and error bars represent the mean and standard deviation of the measurements, respectively.

DFT calculations for propene adsorption through allylic carbon deprotonation predict a contribution deriving from double bond coordination to the surface. Indeed, the adsorption geometry changes and the binding energy significantly weakens if the vinylic contribution is impeded (see Figure S27). The propene stripping experiment in Figure 7 also suggests an active role of the unsaturated carbons in the molecule's coordination with the surface, as indicated by the significant amount of propane desorbing on a cathodic sweep. The propene desorption during the stripping experiment, on the other hand, may represent propene adsorbed through purely allylic coordination. Vinylic adsorption forces the molecule into a flat adsorption geometry, requiring the availability of more surface sites than solely allylic coordination. With the high carbon coverage regimes suggested by DFT under reaction conditions, this cumbersome adsorption mechanism might be hindered, while purely allylic adsorption requiring less surface availability could become relatively more favorable.

To gain insights in the competition between vinyl coordination and other adsorption geometries, we designed and performed a modification of the propene stripping experiment. In these experiments, shown schematically in Figure 8a, and exemplified in Figure 8b, propane desorption is used as a probe for the amount of propene that can adsorb through the vinyl group. The potential at which we dose propene is the same each time, +0.4 V vs RHE, at which no liquid products are formed, and at which the vinyl adsorbate that can be stripped off to propane is at its maximum coverage (Figure 7b). After dosing and purging out the propene, the electrode is scanned cathodic to 0.1 V vs RHE and then anodic up to a cleaning potential which is varied at each time. The portion of strongly-adsorbed species that are oxidized off of the surface as CO₂ increases with increasing cleaning potential (Figure 8c, left y-axis). The cleaning potential thus controls the coverage of the surface prior to the next propene dose. When propene is dosed now, it must compete with the remaining adsorbates for sites. According to our hypothesis, the coverage of vinyl-bound propene resulting from a propene dose that can desorb

as propane on the cathodic scan after the dose should increase with the availability of sites for vinylic coordination, and thus with the cleaning potential. The integrated post-dose propane (C_3H_8) and propene (C_3H_6) is plotted as a function of the cleaning potential in Figure 8c (right y-axis). To ensure that the changing amount of propane is a result of the surface coverage prior to the propene dose, we stepped up the cleaning potential and then repeated a few cleaning potentials stepping down. The post-dose propane follows the pre-dose CO_2 desorption and the cleaning potential. This indicates that adsorption through the vinyl group is inhibited on a highly covered surface, confirming that coverage directs the adsorption geometry. The propene (C_3H_6) desorption on the other hand does not depend on the cleaning potential, indicating that the amount of propene adsorbed exclusively through the allylic carbon is not influenced by the pre-dose coverage.

In our analysis, we do not explicitly consider steps and undercoordinated sites. These sites are more reactive than terraces and therefore we assume under reaction conditions these sites are readily passivated by carbon species and remain poisoned during catalytic activity, without participating in the proposed mechanism. Nevertheless, our results do not allow for definite exclusion of their role in the mechanism.

Allyl alcohol conversion tests

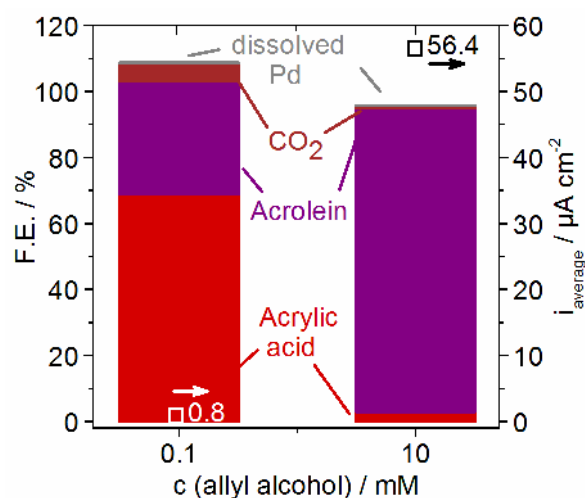


Figure 9 - Product distribution (faradaic efficiency, bar chart) for steady-state oxidation of different concentrations of allyl alcohol in 0.1 M HClO₄ at 0.8 V vs RHE for one hour. The average of the current density over the measurement time period is shown on the right axis (squares).

In the reaction scheme proposed above, the 2-electron partial oxidation product allyl alcohol is considered an intermediate in the production of the 4- and 6-electron partial oxidation products acrolein and acrylic acid. This is motivated by the fact that allyl alcohol has its peak production rate just cathodic of the latter products (Figure 4). To test this hypothesis, we performed direct allyl alcohol oxidation experiments.

Figure 9 shows the average total current density and the faradaic efficiency for direct oxidation of allyl alcohol on Pd at the intermediate potential 0.8 V vs RHE for 60 min. Two different alcohol concentrations were tested; a 0.1 mM solution to represent the approximate concentration of allyl alcohol that was produced during 1 h of propene oxidation, and a 10 mM solution corresponding to the concentration of propene in the propene oxidation experiments. At the low concentration, the average current density was equivalent to the experiments in propene. At high concentration, it was increased more than 50-fold. Interestingly, the lower concentration experiment produced more of the further oxidized acrylic acid (4 e⁻ process) whereas the higher concentration produces more of the less oxidized acrolein (2 e⁻ process). Additional minor products are acrolein or acrylic acid, respectively,

CO₂ and traces of propanal. Dissolution of Pd was observed, but no acetone, as is expected in the absence of propene. The observed high current densities for allyl alcohol oxidation are in agreement with the theoretical hypothesis that oxygen incorporation is the rate determining step.

Discussion

In steady-state propene oxidation experiments, we observed a complex potential dependence of the product distribution and high selectivity towards partial oxidation product acrolein, though with low ECSA-normalized current densities and signs of catalyst degradation. Reaction modelling predicts that on a clean surface the carbon intermediates bind too strongly and degrade rather than incorporate oxygen and convert to products. However, computed energies and propene stripping experiments indicate that the surface coverage of propene-derived species is high under reaction conditions and plays a key role in the adsorption mechanism. Hence, we propose a reaction scheme summarized in Figure 10. At low coverage, lack of spatial constraints promotes flat propene adsorption through combined allyl-vinyl binding. Depending on the potential, this adsorbate can degrade to smaller C_xH_y fractions and/or oxidized further, deprotonating the allyl carbon and sinking into a 3-fold hollow site. DFT predicts these species to be highly stable and not to react further under steady-state, increasing the surface coverage. They can however be stripped off as CO₂ on an anodic sweep. The allyl-vinyl adsorbed propene can be reduced to propane on a cathodic sweep. At high carbon coverages, low site availability restricts the adsorption geometry to be primarily allylic and on atop position. This induces the formation of weakly bound, reactive adsorbates, enabling steady-state conversion to the observed reaction products, though at the price of reduced activity due to partial poisoning. The forced displacement of reactants from a stabilized adsorption configuration to a more unstable, reactive position by surface adsorbates also causes a reduction in kinetic barriers, as shown with DFT. This resembles an effect known from Lindlar-type catalysts for selective hydrogenation of multiply unsaturated alkenes,^{50,51} where partial poisoning of the surface, e.g. by methanol, destabilizes the adsorption of intermediates, preventing full hydrogenation.⁵²

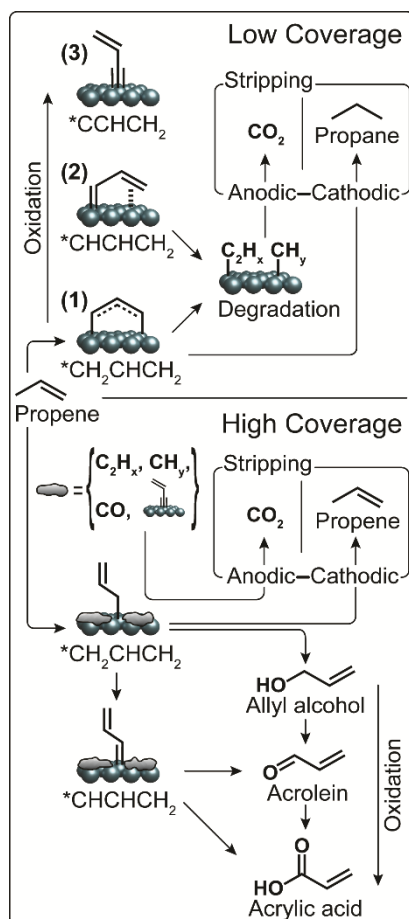


Figure 10 - Graphical representation of the proposed pathways for propene adsorption and conversion. The scheme is divided into two sectors, according to the coverage regime. In each sector, an inset addresses the desorbed species detected in propene stripping experiments.

Interestingly, the propene oxidation product propylene glycol, which requires oxidation of the double bond, is only produced significantly at potentials anodic of 1.0 V vs RHE. This could also be explained as a coverage effect. The lower coverage at high potentials, evidenced by the stripping experiments (Figure 7b), enables coordination of the vinyl group. However, we do not exclude a different adsorption mechanism on an oxidized surface, though an extensive study on such oxidized surfaces is beyond the scope of this work. That said, the direct partial oxidation of propene to propylene glycol is of high industrial interest, since the existing pathways to propylene glycol (via propene oxide) have numerous disadvantages.⁵³

The direct oxidation of allyl alcohol yielded different product concentrations depending on the concentration of allyl alcohol employed. This can be rationalized with a similar mechanistic approach as the oxidation of propene, as illustrated in Figure 11: The adsorption of allyl alcohol is energetically

favored, resulting in a high coverage at high concentrations, but lower coverage at the lower concentration we employed. While surface-bound oxygen species are required for the oxidation to acrylic acid, oxidation to acrolein can also occur by hydroxyl group deprotonation of allyl alcohol. Therefore, at high alcohol coverages, the dominating process will be formation of acrolein, due to the lack of surface oxygen species. At low coverage, surface oxygen species will be available, making way for the direct oxidation to acrylic acid.

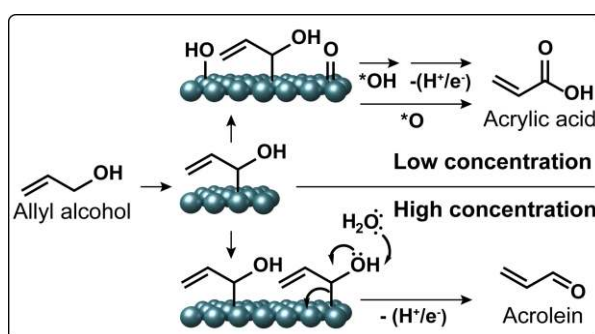


Figure 11 - Proposed mechanism for the oxidation of allyl alcohol at low (0.1 M, top) and high (10 M, bottom) concentration, yielding two different product distributions.

5. Conclusions

In this study, using a combination of theoretical modeling and experimental techniques, we presented an in-depth analysis of propene oxidation on high surface area polycrystalline Pd in 0.1 M HClO₄.

The mechanistic findings in the report are the groundwork to efficient electrochemical conversion of propene. First, in propene oxidation steric effects at the surface regulate the reaction outcome by steering the adsorbate geometry. Thus, it is crucial to tune the catalyst surface population and coverage regimes. Second, with Langmuir-Hinshelwood kinetics on a carbophilic catalyst, the formation of oxygen species at the surface is rate limiting. Balancing oxygen and carbon adsorption while limiting vinylic coordination should ensure higher catalytic turnover, concurrently enabling selectivity towards allylic oxidation products. On the other hand, selective activation of the vinyl group on weaker adsorption sites would promote formation of other industrially relevant products,

propylene oxide and propylene glycol, while minimizing degradation. Third, it is important to improve catalysts stability under oxidative reaction conditions, either by engineering catalysts active at lower potentials, or by synthesis of catalytic materials resistant to anodic corrosion.

Through this work, we outline possible catalyst design strategies for propene partial electro-oxidation reactions and beyond. In practice, one could achieve greater surface coverage control e.g. by deposition of poisoning additives to form different atomic surface ensembles.⁵⁴ Alternatively, we are currently developing intermetallic catalysts embedding carbophilic metals (Pd, Pt, Ru, Rh, Ir) in inert or oxophilic matrices (Ag, Sn, Au, graphite); this should activate specific reactant functionalities without prior poisoning, retaining all the mass activity of the precious metal used. Ultimately, the application of a multi-angle approach as the one presented, and a prudent generalization of our conclusions can support the study of other hydrocarbon partial oxidation reactions.

6. Conflicts of interest

There are no conflicts to declare.

7. Author Contributions

A.W. and L.S. contributed equally. A.W., B.J.S., I.C. and I.E.L.S. designed the bulk electrolysis experiments. A.W. carried out the catalyst preparation, electrochemical experiments and product analysis. K.E.-R. designed and performed NMR characterization of products. S.B.S., D.B.T. and P.C.K.V. and I.C. designed the stripping experiments, S.B.S. carried them out. J.R., L.S., M.S. and P.G.M. designed the DFT study, L.S. carried it out. A.W., L.S. and S.B.S. wrote the manuscript; all authors were involved in discussing and interpreting results and editing the manuscript.

8. Acknowledgements

We gratefully acknowledge the funding by Danmarks Innovationsfonden, part of the ProActive project (5160-00003B) and by Villum Fonden, part of the Villum Center for the Science of Sustainable Fuels and Chemicals (V-SUSTAIN grant 9455). 800 MHz NMR spectra were recorded at the NMR Center at DTU supported by the Villum Foundation.

9. References

- 1 N. S. Lewis and D. G. Nocera, *Proc. Natl. Acad. Sci. U. S. A.*, 2006, **103**, 15729–15735.
- 2 B. Lee, H. Naito, M. Nagao and T. Hibino, *Angew. Chemie - Int. Ed.*, 2012, **51**, 6961–6965.
- 3 M. T. M. Koper, in *Catalysis in Chemistry and Biology*, World Scientific, 2018, pp. 229–232.
- 4 C. Reller, R. Krause, E. Volkova, B. Schmid, S. Neubauer, A. Rucki, M. Schuster and G. Schmid, *Adv. Energy Mater.*, 2017, **7**, 1602114.
- 5 N. Agarwal, S. J. Freakley, R. U. McVicker, S. M. Althahban, N. Dimitratos, Q. He, D. J. Morgan, R. L. Jenkins, D. J. Willock, S. H. Taylor, C. J. Kiely and G. J. Hutchings, *Science (80-.)*, 2017, **358**, 223–227.
- 6 Z. Liang, T. Li, M. Kim, A. Asthagiri and J. F. Weaver, *Science (80-.)*, 2017, **356**, 299–303.
- 7 K. T. Dinh, M. M. Sullivan, P. Serna, R. J. Meyer, M. Dincă and Y. Román-Leshkov, *ACS Catal.*, 2018, 8306–8313.
- 8 A. Marimuthu, J. Zhang and S. Linic, *Science (80-.)*, 2013, **339**, 1590–1593.
- 9 M. D. Hughes, Y.-J. Xu, P. Jenkins, P. McMorn, P. Landon, D. I. Enache, A. F. Carley, G. A. Attard, G. J. Hutchings, F. King, E. H. Stitt, P. Johnston, K. Griffin and C. J. Kiely, *Nature*, 2005, **437**, 1132–1135.
- 10 B. K. Min and C. M. Friend, *Chem. Rev.*, 2007, **107**, 2709–2724.
- 11 Y. Choi, I. Sinev, H. Mistry, I. Zegkinoglou and B. Roldan Cuenya, *ACS Catal.*, 2016, **6**, 3396–3403.
- 12 Z. W. Seh, J. Kibsgaard, C. F. Dickens, I. Chorkendorff, J. K. Nørskov and T. F. Jaramillo, *Science (80-.)*, 2017, **355**, eaad4998.
- 13 B. Lee and T. Hibino, *J. Catal.*, 2011, **279**, 233–240.
- 14 M. E. O'Reilly, R. S. Kim, S. Oh and Y. Surendranath, *ACS Cent. Sci.*, 2017, 2–7.
- 15 N. Danilovic, K. E. Ayers, C. Capuano, J. N. Renner, L. Wiles and M. Pertoso, *ECS Trans.*, 2016, **75**, 395–402.
- 16 S. J. Khatib and S. T. Oyama, *Catal. Rev.*, 2015, **57**, 306–344.
- 17 P. Sprenger, W. Kleist and J.-D. Grunwaldt, *ACS Catal.*, 2017, **7**, 5628–5642.
- 18 Nexant, *Nexant Petroleum and Petrochemical Economics (PPE) Program*, 2017.
- 19 C. J. Sullivan, A. Kuenz and K.-D. Vorlop, in *Ullmann's Encyclopedia of Industrial Chemistry*, Wiley-VCH Verlag GmbH & Co. KGaA, Weinheim, Germany, 2018, pp. 1–15.
- 20 M. Weber, W. Pompeckzi, R. Bonmann and M. Weber, in *Ullmann's Encyclopedia of Industrial Chemistry*, Wiley-VCH Verlag GmbH & Co. KGaA, Weinheim, Germany, 2014, pp. 1–19.
- 21 J. O. Bockris, H. Wroblowa, E. Gileadi and B. J. Piersma, *Trans. Faraday Soc.*, 1965, **61**, 2531–2545.
- 22 M. Bełtowska-Brzezinska, T. Łuczak, H. Baltruschat and U. Müller, *J. Phys. Chem. B*, 2003, **107**, 4793–4800.
- 23 T.-C. Chou and J.-C. Chang, *Chem. Eng. Sci.*, 1980, **35**, 1581–1590.
- 24 K. Scott, C. Odouza and W. Hui, *Chem. Eng. Sci.*, 1992, **47**, 2957–2962.
- 25 G. Göransson, J. S. Jirkovský, P. Krtil and E. Ahlberg, *Electrochim. Acta*, 2014, **139**, 345–355.

- 26 L. L. Holbrook and H. Wise, *J. Catal.*, 1975, **38**, 294–298.
- 27 V. M. Schmidt and E. Pastor, *J. Electroanal. Chem.*, 1996, **401**, 155–161.
- 28 G. R. Stafford, *Electrochim. Acta*, 1987, **32**, 1137–1143.
- 29 K. Otsuka, Y. Shimizu, I. Yamanaka and T. Komatsu, *Catal. Letters*, 1989, **3**, 365–370.
- 30 N. Markovic, *J. Electrochem. Soc.*, 1997, **144**, 1591.
- 31 R. Ojani, E. Hasheminejad and J. B. Raoof, *Int. J. Hydrogen Energy*, 2014, **39**, 8194–8203.
- 32 J. Liu, L. Cao, W. Huang and Z. Li, *J. Electroanal. Chem.*, 2012, **686**, 38–45.
- 33 E. Bertheussen, T. V. Hogg, Y. Abghoui, A. K. Engstfeld, I. Chorkendorff and I. E. L. Stephens, *ACS Energy Lett.*, 2018, **3**, 634–640.
- 34 D. B. Trimarco, S. B. Scott, A. H. Thilsted, J. Y. Pan, T. Pedersen, O. Hansen, I. Chorkendorff and P. C. K. Vesborg, *Electrochim. Acta*, 2018, **268**, 520–530.
- 35 J. Enkovaara, C. Rostgaard, J. J. Mortensen, J. Chen, M. Duřak, L. Ferrighi, J. Gavnholt, C. Glinsvad, V. Haikola, H. A. Hansen, H. H. Kristoffersen, M. Kuisma, A. H. Larsen, L. Lehtovaara, M. Ljungberg, O. Lopez-Acevedo, P. G. Moses, J. Ojanen, T. Olsen, V. Petzold, N. A. Romero, J. Stausholm-Møller, M. Strange, G. A. Tritsarlis, M. Vanin, M. Walter, B. Hammer, H. Häkkinen, G. K. H. Madsen, R. M. Nieminen, J. K. Nørskov, M. Puska, T. T. Rantala, J. Schiøtz, K. S. Thygesen and K. W. Jacobsen, *J. Phys. Condens. Matter*, 2010, **22**, 253202.
- 36 A. Hjorth Larsen, J. Jørgen Mortensen, J. Blomqvist, I. E. Castelli, R. Christensen, M. Duřak, J. Friis, M. N. Groves, B. Hammer, C. Hargus, E. D. Hermes, P. C. Jennings, P. Bjerre Jensen, J. Kermode, J. R. Kitchin, E. Leonhard Kolsbjerg, J. Kubal, K. Kaasbjerg, S. Lysgaard, J. Bergmann Maronsson, T. Maxson, T. Olsen, L. Pastewka, A. Peterson, C. Rostgaard, J. Schiøtz, O. Schütt, M. Strange, K. S. Thygesen, T. Vegge, L. Vilhelmsen, M. Walter, Z. Zeng and K. W. Jacobsen, *J. Phys. Condens. Matter*, 2017, **29**, 273002.
- 37 S. R. Bahn and K. W. Jacobsen, *Comput. Sci. Eng.*, 2002, **4**, 56–66.
- 38 M. Hara, U. Linke and T. Wandlowski, *Electrochim. Acta*, 2007, **52**, 5733–5748.
- 39 F. Hernandez and H. Baltruschat, *Langmuir*, 2006, **22**, 4877–4884.
- 40 N. Hoshi, K. Kagaya and Y. Hori, *J. Electroanal. Chem.*, 2000, **485**, 55–60.
- 41 N. Hoshi, M. Kuroda and Y. Hori, *J. Electroanal. Chem.*, 2002, **521**, 155–160.
- 42 M. Pourbaix, *Atlas of electrochemical equilibria in aqueous solutions*, Pergamon Press, 1974.
- 43 P. Y. Bruice, *Organic Chemistry*, Pearson Education, 2007.
- 44 J. K. Nørskov, J. Rossmeisl, A. Logadottir, L. Lindqvist, J. R. Kitchin, T. Bligaard and H. Jónsson, *J. Phys. Chem. B*, 2004, **108**, 17886–17892.
- 45 K. J. J. Mayrhofer, M. Arenz, B. B. Blizanac, V. Stamenkovic, P. N. Ross and N. M. Markovic, *Electrochim. Acta*, 2005, **50**, 5144–5154.
- 46 M. T. M. Koper, S. C. S. Lai and E. Herrero, in *Fuel Cell Catalysis*, John Wiley & Sons, Inc., Hoboken, NJ, USA, 2009, pp. 159–207.
- 47 L. Vitos, A. V. Ruban, H. L. Skriver and J. Kollár, *Surf. Sci.*, 1998, **411**, 186–202.
- 48 E. Pastor, S. Wasmus, T. Iwasita, M. C. Arévalo, S. Gonzalez and A. J. Arvia, *J. Electroanal. Chem.*, 1993, **353**, 81–100.
- 49 M. C. Arévalo, J. L. Rodríguez and E. Pastor, *J. Electroanal. Chem.*, 2001, **505**, 62–71.
- 50 H. Lindlar, *Helv. Chim. Acta*, 1952, **35**, 446–450.

- 51 D. Albani, M. Shahrokhi, Z. Chen, S. Mitchell, R. Hauert, N. López and J. Pérez-Ramírez, *Nat. Commun.*, 2018, **9**, 2634.
- 52 G. Horányi and K. Torkos, *J. Electroanal. Chem. Interfacial Electrochem.*, 1980, **111**, 279–286.
- 53 T. A. Nijhuis, M. Makkee, J. A. Moulijn and B. M. Weckhuysen, *Ind. Eng. Chem. Res.*, 2006, **45**, 3447–3459.
- 54 D. Strmcnik, M. Escudero-Escribano, K. Kodama, V. R. Stamenkovic, A. Cuesta and N. M. Marković, *Nat. Chem.*, 2010, **2**, 880–885.